frontiers | Frontiers in Marine Science

TYPE Original Research
PUBLISHED 28 March 2023
DOI 10.3389/fmars.2023.1166305

OPEN ACCESS

EDITED BY
Min Luo,
Shanghai Ocean University, China

REVIEWED BY
Xiaoming Sun,
Sun Yat-sen University, China
Giuliana Panieri,
UiT the Arctic University of Norway, Norway

*CORRESPONDENCE
Jiasheng Wang
js-wang@cug.edu.cn

SPECIALTY SECTION
This article was submitted to Marine Biogeochemistry, a section of the journal Frontiers in Marine Science

RECEIVED 15 February 2023
ACCEPTED 16 March 2023
PUBLISHED 28 March 2023

CITATION
Cen Y, Wang J, Algeo TJ, Wang Z, Ma X and Chen C (2023) Methane release effects on foraminiferal tests in northern South China Sea.
Front. Mar. Sci. 10:1166305.
doi: 10.3389/fmars.2023.1166305

Methane release effects on foraminiferal tests in northern South China Sea

Yue Cen[1,2], Jiasheng Wang[1,2]*, Thomas J. Algeo[1,3,4], Zhou Wang[1,2,5], Xiaochen Ma[1,2] and Can Chen[1,2]

[1]Hubei Key Laboratory of Marine Geological Resources in College of Marine Science and Technology, China University of Geosciences, Wuhan, Hubei, China, [2]State Key Laboratory of Biogeology and Environment Geology, China University of Geosciences, Wuhan, Hubei, China, [3]State Key Laboratory of Geological Processes and Mineral Resources, China University of Geosciences, Wuhan, Hubei, China, [4]Department of Geosciences, University of Cincinnati, Cincinnati, OH, United States, [5]State Key Laboratory of Marine Geology, Tongji University, Shanghai, China

Upward diffusing methane in gas hydrate geological systems is consumed in the sediment and water column by a series of biogeochemical reactions, which not only affect living foraminifera but also lead to early diagenetic alteration of buried foraminiferal tests. Previous studies of the impact of methane release events on fossil foraminifera focused mainly on carbon and oxygen isotopes, with little attention given to other geochemical proxies to date. Here, we examine the test wall microstructure and analyze the elemental and stable carbon-oxygen isotopic compositions of buried foraminifera from gas hydrate-bearing sediments at Site GMGS2-16 in the northern South China Sea. Our results show that diagenetic alteration of foraminiferal tests at Site GMGS2-16 is mainly linked to high-Mg calcite overgrowths. Test $\delta^{13}C$ covaries negatively with the degree of diagenetic alteration (based on petrographic characteristics) but positively with Mg/Ca ratios. With increasing diagenetic alteration, Ba/Ca, Mn/Ca, Fe/Ca, Mo/Ca, U/Ca, V/Ca, Ni/Ca and Co/Ca also generally increase, but Sr/Ca and Cu/Ca exhibit variable changes. We infer that foraminiferal tests are highly susceptible to alteration by methane-bearing fluids, and that the elemental ratios of diagenetically altered tests are potentially reliable proxies for paleo-methane release events. At Site GMGS2-16, the overall pattern of diagenetic alteration of foraminiferal tests records frequent vertical fluctuations of the sulfate-methane transition zone (SMTZ) caused by variable fluid flux and methane release rates, with two discrete large-scale methane release events having maximum ages of ~0.47 ka and ~170 ka.

KEYWORDS

carbon isotopes, oxygen isotopes, early diagenesis, LA-ICP-MS, trace elements, gas hydrates

1 Introduction

A large amount of methane is trapped as methane hydrates, dissolved methane and free gas reservoirs in continental margin sediments worldwide. Methane-rich fluids can migrate upwards along faults and fractures, emitting methane back into the hydrosphere and atmosphere, which can have serious impacts on global climate and the biosphere (Dickens et al., 1997; Retallack et al., 1998; Them et al., 2018). Hence, it is of considerable importance to evaluate the character, timing, and drivers of natural past methane release events and explore how to avoid consequent climatic and biotic effects (Miao et al., 2021). Methane-derived authigenic carbonate (MDAC) is regarded as a reliable archive of information about paleo-methane release events, past fluid composition and circulation, and sedimentary redox processes (Peckmann and Thiel, 2004; Feng et al., 2009; Hu et al., 2015; Crémière et al., 2016; Liang et al., 2017; Zhu et al., 2019; Bayon et al., 2020; Schier et al., 2021; Liu et al., 2022). During the upward migration of methane-bearing fluids, steep chemical gradients provide ecological niches for microbial communities mediating the anaerobic oxidation of methane (AOM, $CH_4 + SO_4^{2-} \rightarrow HCO_3^- + HS^- + H_2O$) in the sulfate-methane transition zone (SMTZ). The production of bicarbonate results in increased pore-fluid alkalinity, inducing precipitation of MDAC at timescales typically in the range of centuries to millennia (Schneider, 2018). Therefore, some short duration paleo-methane release events may fail to leave a carbonate record.

Diagenetically altered foraminifera have been found to preserve post-depositional signals similar to those in MDAC (Torres et al., 2010), and the wider distribution of the former therefore has the potential to yield higher-resolution records of paleo-methane release events. Organic matter in marine sediments is subject to a succession of heterotrophic microbial metabolisms that utilize a depth sequence of electron acceptors, largely in accordance with Gibbs free energy yield: NO_3^-, Mn(IV), Fe(III), and SO_4^{2-} (Jørgensen, 2021). When all energetically more favorable terminal electron acceptors have been depleted, organic carbon is mineralized *via* methanogenesis, causing the accumulation of methane in deeper sediments. Upward diffusing methane will meet the zone of sulfate reduction and AOM occurs. The diagenetic processes not only affect living benthic foraminifera but also lead to diagenetic alteration of buried foraminiferal tests (Millo et al., 2005a; Torres et al., 2010; Panieri et al., 2017; Schneider et al., 2017; Cen et al., 2022). To date, most studies investigating the effect of methane release events on foraminiferal tests have focused on their stable carbon isotopic compositions (Hill et al., 2004; Millo et al., 2005b; Martin et al., 2007; Panieri et al., 2014; Schneider et al., 2017; Sztybor and Rasmussen, 2017; Wan et al., 2018). Additionally, their elemental compositions (e.g., Mg/Ca, Sr/Ca, Ba/Ca, Mn/Ca, Fe/Ca, U/Ca, and Al/Ca) (Torres et al., 2010; Schneider et al., 2017; Fontanier et al., 2018; Detlef et al., 2020) may also be influenced by MDAC precipitation. Borrelli et al. (2020) proposed benthic foraminiferal $\delta^{34}S$ as a novel tool to identify methane release events in geological records and to indirectly date fossil seeps. Nonetheless, a comprehensive understanding of the influence of early diagenetic processes on the elemental composition of foraminifera awaits the analysis of a full suite of elemental ratios in a suitably designed study.

Here, we undertook a suite of petrographic and geochemical analyses including reflected light microscopy, scanning electron microscope (SEM) imaging, oxygen and carbon isotopic measurements, laser ablation inductively coupled plasma mass spectrometry (LA-ICP-MS), and electron probe microanalysis (EPMA) elemental mapping on foraminiferal tests with varying degrees of diagenetic alteration from gas hydrate-bearing sediments of the northern South China Sea. Our main goal was to investigate the effects of methane release on diagenetic alteration of foraminiferal tests and to refine multiple proxies for recognition of paleo-methane release events in gas hydrate geosystems.

2 Geological setting

The South China Sea (SCS) is one of the largest marginal seas in the western Pacific Ocean (Taylor and Hayes, 1980). On account of the interactive and complex collision among the Eurasian, Pacific and Indian-Australian plates, a series of sedimentary basins, e.g., the Qiongdongnan Basin and Pearl River Mouth Basin, were developed along the northern continental margin of the SCS (Zhu et al., 2009; Morley, 2012). During June to September in 2013, the gas hydrate drilling expedition GMGS2 was conducted by the Chinese Geological Survey (CGS) incorporating with Fugro and Geotek to accurately quantify gas hydrate in the sediment cores and to determine the nature and distribution of gas hydrate within the sedimentary sequence in the Pearl River Mouth Basin (Zhang et al., 2015). The drilling area of expedition GMGS2 was located in the eastern Pearl River Mouth Basin, along the crest of two prominent seafloor ridges (Figure 1), where bottom simulating reflectors and other seismic indicators for widespread gas hydrate and seepage had been recognized (Zhang et al., 2015).

The study site (GMGS2-16), which is located on the eastern ridge (Figure 1) at a water depth of 871 m, yielded a 230-m-long core. The age framework for site GMGS2-16 was established by combining calcareous nannofossil and planktonic foraminifer datums (Chen et al., 2016a). The oldest sediments recovered are

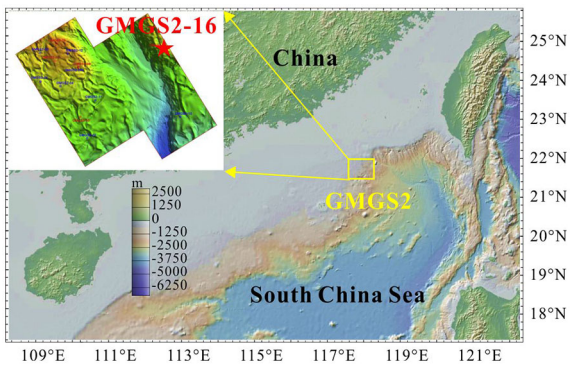

FIGURE 1
Location of the study site (GMGS2-16) in the eastern Pearl River Mouth Basin, South China Sea (modified after Zhang et al., 2015).

of middle Pleistocene age, younger than ~500 ka. Sedimentation rates since 440 ka have varied from 28 to 62.3 cm/kyr, with a mean rate of 47.4 cm/kyr (Chen et al., 2016a). The logging-while-drilling data indicated the existence of two layers of gas hydrate: an upper hydrate layer, characterized by nodules and fracture-filling hydrates, at a shallow depth (13-29 mbsf), and a lower pore-filling hydrate layer near the bottom simulating reflector (BSR) at depths of 192-222 mbsf (Feng et al., 2015). At this site, porewater sulfate concentrations decline to zero at 13.69 mbsf, indicating a high upward methane flux and a shallow SMTZ (Kuang et al., 2018).

3 Materials and methods

3.1 Sample description and processing

The dominant lithologies of the sediments in this core are dark-green, unconsolidated clayey silt and silty clay. Authigenic minerals including carbonate, pyrite, and gypsum were observed at multiple levels (Gong et al., 2017; Lin et al., 2018; Zhao et al., 2021). For this study, sediment samples were collected from the curated core at the GMGS laboratory in Guangzhou and processed in the State Key Laboratory of Biogeology and Environmental Geology (BGEG) at China University of Geosciences in Wuhan (CUG). Fifty-seven core samples, each representing a quarter-section of the drillcore having a volume of 10-15 cm^3, were collected, weighed, and stored in a freezer prior to analysis. For each sample, a ~10 cm^3 aliquot was dried at 40 °C for 24 hours in an air-dry oven and re-weighed to determine moisture-free sample weight. This aliquot was then rinsed using distilled water, sieved through 150 μm, 65 μm and 30.8 μm sifters. In the process of sieving, the sample was ultrasonicated in distilled water for 30 s to remove clay minerals and detrital materials sticking to the foraminiferal tests. For each sample, the three size fractions were air dried at a temperature of 40 °C, and then stored separately after weighing.

3.2 Petrography

All particles with size of larger than 150 μm were examined using a binocular microscope (Carl Zeiss Stemi 2000-C). Foraminiferal samples were grouped into four classes (pristine, weakly altered, moderately altered, and strongly altered; Figure 2) according to their degree of diagenetic alteration following the approach of Schneider et al. (2017). Well-preserved pristine tests are optically smooth with high reflectance and transparency, and primary test features such as chambers, sutures and pores are easily observed. Weakly altered tests are translucent or white in color with decreased reflectance and transparency, but still have prominent morphological features. Moderately altered tests appear white or yellow with both translucent and opaque areas. Strongly altered tests appear yellow to dark brown in color, low reflectance and transparency with an opaque test wall, a 'frosty' texture, and obscured morphological features. In order to determine the frequencies of the various diagenetic alteration stages, all foraminiferal specimens larger than 150 μm in each core sample were assigned to one of these four categories and tallied. Given their relatively greater abundance, three foraminiferal species were chosen for geochemical measurements: the planktic taxa *Globorotalia menardii* and *Neogloboquadrina dutertrei*, and the benthic taxon *Uvigerina peregrina*.

3.3 Scanning electron microscopy

Representative foraminiferal tests of each species (i.e., *G. menardii*, *N. dutertrei*, and *U. peregrina*) at each diagenetic alteration stage (as determined by reflected-light microscopy) were selected from seven core samples and further tested using SEM and elemental analysis (Table 1). The seven core samples cover the intervals containing authigenic carbonate nodules above (GMGS2-16B-1H-1a, 0.23 mbsf), within (GMGS2-16D-2H-1, 10.83 mbsf), and below (GMGS2-16F-6H-1, 50.47 mbsf; GMGS2-16D-8H-1, 92.32 mbsf; GMGS2-16H-4H-1b, 164.68 mbsf) the current SMTZ (the bottom boundary is at 13.69 mbsf) (Kuang et al., 2018), as well as some intervals where no authigenic carbonate nodules are present (GMGS2-16F-2P-CC, 20.52 mbsf; GMGS2-16F-5H-2, 40.92 mbsf), with the aim of achieving a comprehensive understanding of the influence of diagenetic processes on foraminiferal geochemistry.

We selected foraminiferal tests of the same species that had approximately equal shell size in order to limit the size dependency of the shell chemistry (Friedrich et al., 2012). The selected specimens were then cleaned ultrasonically with methanol for 10 s to remove clay minerals and other particles, with repeated rinses performed until visible discoloration was absent. Then each specimen was mounted in epoxy resin and polished down to yield a cross-section view for the purpose of studying its internal structure. SEM observation and imaging were conducted on whole and polished specimens of tests using a Hitachi SU8010 SEM in high-vacuum mode, with a beam voltage of 10-20 kV, at the State Key Laboratory of BGEG (CUG-Wuhan).

3.4 Geochemical analyses

Foraminiferal $\delta^{13}C$ and $\delta^{18}O$ were measured using a Gas Bench coupled with a Thermo Finnigan MAT 253 at the Oxy-Anion Stable Isotope Consortium (OASIC) in the Department of Geology & Geophysics, Louisiana State University. Each isotopic sample contained 2-3 foraminiferal tests to generate sufficient material for measurement. Samples were loaded into 12 mL Labco Exetainer vials and left in an oven for 12-24 h at 75 °C, then were sealed with Labco septa and flushed with 99.999% helium and manually acidified at 72°C. The carbon dioxide analytic gas was isolated *via* gas chromatography, and water was removed using a Nafion trap prior to introduction into the stable isotope mass spectrometer fitted with a continuous flow interface. Isotopic results are expressed in the delta notation as per mille (‰) deviations from the Vienna-Pee Dee Belemnite (VPDB) standard. Precision was routinely < 0.06 ‰ for $\delta^{13}C$ and < 0.08 ‰ for $\delta^{18}O$.

10.3389/fmars.2023.1166305

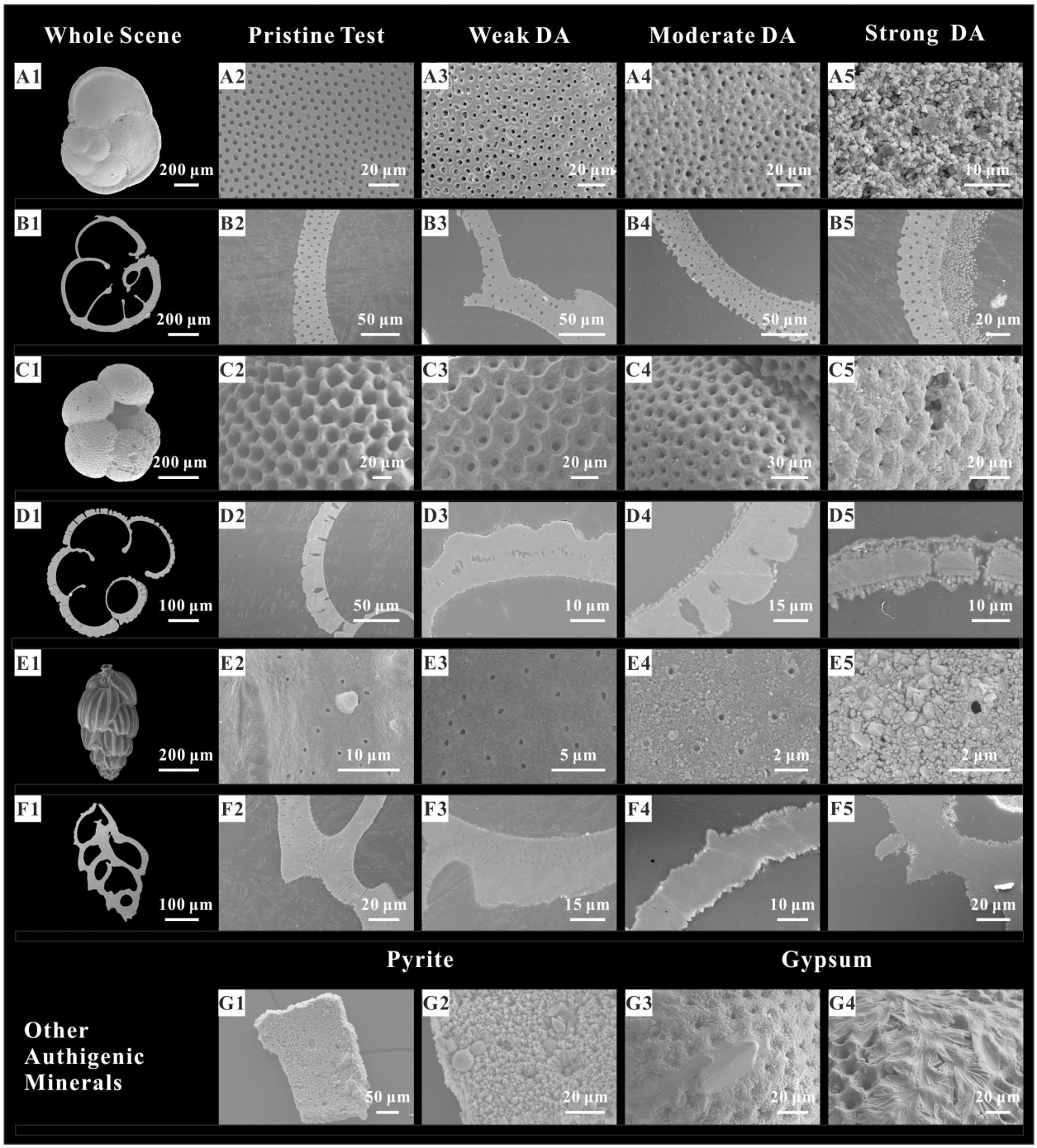

FIGURE 2
SEM images of foraminiferal tests representing a range of diagenetic alteration (DA) stages. Whole test, exterior wall, and wall cross-section views for *G. menardii* (**A**1-**B**5), *N. dutertrei* (**C**1-**D**5), and *U. peregrina* (**E**1-**F**5). Authigenic pyrite framboids inside the test chamber (**G** 1-2), and authigenic gypsum growing on the exterior wall (**G**3-4).

LA-ICP-MS was performed on polished cross-sections of the selected tests. The isotopes of ^{24}Mg, ^{27}Al, ^{43}Ca, ^{51}V, ^{55}Mn, ^{57}Fe, ^{59}Co, ^{60}Ni, ^{63}Cu, ^{88}Sr, ^{97}Mo, ^{137}Ba, ^{238}U were measured along the laser profile tracks. Analyses were measured using an integrated *in situ* laser ablation (COMPexPro 102 ArF 193 nm excimer laser; Coherent GeoLasPro) and ICP-MS (Agilent 7900) system at the Sample-Solution Analytical Technology Co. in Wuhan, China. The spot size and frequency of the laser were set to 44 µm and 5 Hz, respectively. Internal standard-independent calibrations followed the procedure of Chen et al. (2011). Each test session analyzed 50 sample spots, with measurement of a standard (NIST 610) for drift correction after every fifth sample. A series of standard materials were

10.3389/fmars.2023.1166305

TABLE 1 Overview of the analytical techniques for each sample.

Sample ID	Depth (mbsf)	Foraminiferal taxon	Degree of diagenetic alteration (DA)	Methodology			
				SEM	EPMA	$\delta^{13}C$ and $\delta^{18}O$	LA-ICP-MS
GMGS2-16B-1H-1a	0.23	*G. menardii*	Pristine test	√		√	√
			Weak DA	√		√	√
			Moderate DA	√		√	√
			Strong DA	√		√	√
		N. dutertrei	Pristine test	√		√	√
			Weak DA	√		√	√
			Moderate DA	√		√	√
			Strong DA	√		√	√
		U. peregrina	Pristine test	√		√	√
			Weak DA	√		√	√
			Moderate DA	√		√	√
			Strong DA	√		√	√
GMGS2-16D-2H-1	10.83	*G. menardii*	Pristine test			√	√
			Weak DA	√		√	√
			Moderate DA	√		√	√
			Strong DA	√	√	√	√
		N. dutertrei	Pristine test			√	√
			Weak DA	√		√	√
			Moderate DA	√		√	√
			Strong DA	√	√	√	√
		U. peregrina	Pristine test			√	√
			Weak DA	√		√	√
			Moderate DA	√		√	√
			Strong DA	√	√	√	√
GMGS2-16F-2P-CC	20.52	*G. menardii*	Pristine test	√		√	√
		N. dutertrei	Pristine test	√		√	√
		U. peregrina	Pristine test	√		√	√
GMGS2-16F-5H-2	40.92	*G. menardii*	Pristine test			√	√
		N. dutertrei	Pristine test			√	√
		U. peregrina	Pristine test			√	√
GMGS2-16F-6H-1	50.47	*G. menardii*	Pristine test			√	√
			Weak DA	√		√	√
			Moderate DA	√		√	√
		N. dutertrei	Pristine test			√	√
			Weak DA	√		√	√
			Moderate DA	√		√	√
		U. peregrina	Pristine test			√	√

(Continued)

10.3389/fmars.2023.1166305

TABLE 1 Continued

Sample ID	Depth (mbsf)	Foraminiferal taxon	Degree of diagenetic alteration (DA)	Methodology			
				SEM	EPMA	$\delta^{13}C$ and $\delta^{18}O$	LA-ICP-MS
			Weak DA	√		√	√
			Moderate DA	√		√	√
GMGS2-16D-8H-1	92.32	*G. menardii*	Pristine test			√	√
			Weak DA			√	√
			Moderate DA			√	√
			Strong DA			√	√
		N. dutertrei	Pristine test			√	√
			Weak DA			√	√
			Moderate DA			√	√
			Strong DA			√	√
		U. peregrina	Pristine test			√	√
			Weak DA			√	√
			Moderate DA			√	√
			Strong DA			√	√
GMGS2-16H-4H-1b	164.68	*G. menardii*	Pristine test				√
			Weak DA				√
			Moderate DA				√
			Strong DA				√
		N. dutertrei	Pristine test				√
			Weak DA				√
			Moderate DA				√
			Strong DA				√
		U. peregrina	Pristine test				√
			Weak DA				√
			Moderate DA				√
			Strong DA				√

measured before (NIST610, BHVO-2G, BIR-1G, BCR-2G, MACS-3, and MACS-3 in order) and after (same measured in reverse order) the session to set a calibration curve. Each spot analysis incorporated an initial <5 s wash-out time then ~20 s background acquisition, followed by a ~50 s sample-data acquisition interval. ICPMSDataCal (version 10.8) software was used to calculate and calibrate off-line data (Liu et al., 2008). For each sample, the reported Element/Ca ratios were calculated by averaging 15-25 measurements (5 laser spots per specimen, 3-5 specimens per sample) to reduce the impact of natural geochemical heterogeneity in foraminiferal tests (Rathmann et al., 2004). The signals of Mn and Al were used to monitor clay contamination, and any specimens with values above 1 mmol/mol (Mn/Ca) or 0.25 mmol/mol (Al/Ca) were removed from the dataset (Skinner et al., 2019).

To study the spatial cross-sectional distribution of Mg in the altered specimens, EPMA elemental mapping were obtained with a JEOL JXA-8230 electron microprobe at the Sample-Solution Analytical Technology Co. in Wuhan, China. Operation conditions were 15 kV acceleration voltage and 20 nA beam current with 1 μm beam diameter. Standards were natural minerals from international suppliers. Before measuring elemental concentrations, optical microscope and SEM images were taken to assess diagenetic alteration and assist in selecting sampling points.

Pairwise correlations among foraminiferal elemental proxies measured by LA-ICP-MS were tested using Pearson correlation coefficients. To test differences in the mean elemental contents of foraminiferal tests, a Student's *t*-test was performed for sample pairs.

4 Results

4.1 Foraminiferal preservation and petrography

Petrographic observation of the core samples using reflected light microscopy revealed that both planktonic and benthic foraminiferal tests exhibit diagenetic alteration features. Each foraminiferal specimen was assigned to one of four categories: pristine, weakly altered, moderately altered, or strong altered (Figure 2). For each core sample, the number of tests assigned to each category was tabulated (Appendix 1). Altered foraminiferal tests are present through nearly the full drillcore, at depths ranging from 0.23 to 205.82 mbsf. The samples yielding the highest percentage of altered tests (>30%) are at depths of 10.83 and 92.32 mbsf, but a larger number of samples contain at least 10% altered tests, including those at 16.65, 22.08, 50.47, and 164.68 mbsf. The samples containing the fewest altered foram tests (<1%) are at 25.73, 29.91, 59.48, 109.75, 148.63-154.63, 172.93, 179.67, 192.46, and 205.82 mbsf. The intensity of diagenetic alteration is variable, e.g., the sample at 10.83 mbsf is dominated by moderately altered tests and the sample at 22.08 mbsf by weakly altered tests. There is no systematic downhole increase in the intensity of diagenetic alteration at site GMGS2-16, challenging the conventional view that diagenetic intensity correlates with burial depth (Schlanger and Douglas, 1974).

SEM microscopy was used to identify various alteration features, including dissolution, overgrowth, and recrystallization (Edgar et al., 2015). SEM imaging reveals that the foraminiferal tests exhibit a range of diagenetic features, including overgrowths of coarse inorganic crystallites, without recrystallization and dissolution. As shown in Figure 2, the internal and external wall surfaces of pristine tests are smooth and free of infilling and overgrowths, pores are unplugged, and wall cross sections are homogeneous with a well-defined outline (Figures 2A2–F2). In contrast to pristine tests, altered tests reveal a fine (~1-30 μm thick) layer of calcite crystals on the tests (Figures 2A 3–F5). The secondary calcite crystals encrust interior and/or exterior test surfaces as well as fill in pores, resulting in a reduction in pore size until complete infilling is achieved. The euhedral crystals grow perpendicular to test walls and are typically much larger than primary foraminiferal biogenic crystals, making them easily identified by SEM. Furthermore, authigenic pyrite (Figures 2G1–2) and gypsum (Figures 2G3–4) were also found inside and outside test chambers.

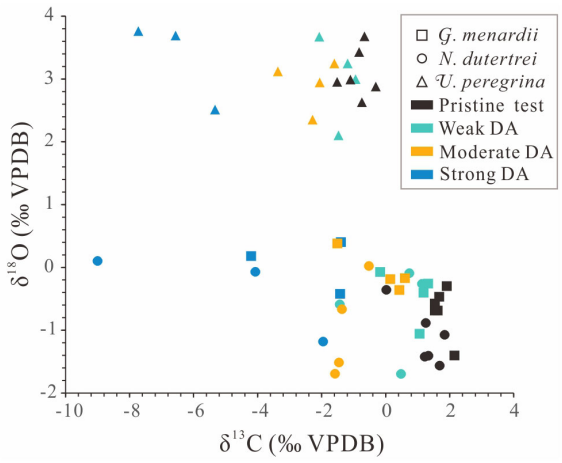

FIGURE 3
Carbon and oxygen stable isotopes of foraminiferal tests at variable diagenetic alteration stages. The squares, circles, and triangles represent the taxa *G. menardii*, *N. dutertrei* and *U. peregrina*, respectively; black, green, orange and blue represent pristine, weakly altered, moderately altered, and strongly altered tests, respectively.

4.2 Stable isotopic compositions

The pristine and altered tests exhibit significantly different carbon isotopic compositions. The pristine tests of *G. menardii*, *N. dutertrei* and *U. peregrina* exhibit $\delta^{13}C$ values ranging from +1.53 ‰ to +1.66 ‰, +1.21 ‰ to +1.83 ‰, and −0.75 ‰ to −0.31 ‰, respectively (Figure 3, Table 2, Appendix 2). In contrast, foraminiferal tests of *G. menardii*, *N. dutertrei* and *U. peregrina* with variable diagenetic alteration stages have $\delta^{13}C$ values ranging

TABLE 2 Overall range and average value of carbon and oxygen stable isotopes for samples with weak, moderate, and strong diagenetic alteration.

	Degree of diagenetic alteration (DA)	*G. menardii*			*N. dutertrei*			*U. peregrina*		
		min	max	average	min	max	average	min	max	average
$\delta^{13}C$ (‰ VPDB)	Pristine test	+1.52	+2.14	+1.73	+0.01	+1.83	+1.21	−1.52	−0.31	−0.87
	Weak DA	−0.18	+1.31	+0.84	−1.44	+1.12	+0.22	−2.08	−0.95	−1.43
	Moderate DA	−1.52	+0.59	−0.10	−1.59	−0.53	−0.96	−3.37	−1.61	−2.33
	Strong DA	−4.21	−1.40	−2.35	−8.99	−1.96	−5.01	−7.72	−5.33	−6.54
$\delta^{18}O$ (‰ VPDB)	Pristine test	−1.41	−0.30	−0.69	−1.57	−0.36	−1.12	+2.63	+3.68	+3.09
	Weak DA	−1.06	−0.08	−0.45	−1.70	−0.09	−0.66	+2.10	+3.67	+3.00
	Moderate DA	−0.36	+0.38	−0.09	−1.69	+0.02	−0.96	+2.35	+3.25	+2.91
	Strong DA	−0.42	+0.40	+0.05	−1.18	+0.10	−0.38	+2.51	+3.76	+3.32

from −1.52 ‰ to +1.59 ‰, −8.99 ‰ to +1.32 ‰ and −7.72 ‰ to −0.95 ‰, respectively. As can be seen from Figure 3 and Table 2, with the increase of diagenetic alteration, the range of carbon isotopes tends to be wider and the boundary values of the range as well as the average $\delta^{13}C$ value of both planktonic and benthic foraminiferal tends to be more negative.

The oxygen isotopic compositions of the pristine and altered tests do not differ as significantly as the carbon isotopic composition. The $\delta^{18}O$ values of pristine tests are less variable ranging from −0.57 ‰ to −0.30 ‰ for planktonic foraminifera (*G. menardii* and *N. dutertrei*) and +2.63 ‰ to +3.68 ‰ for benthic foraminifera (*U. peregrina*) (Table 2). On the other hand, the foraminiferal tests of planktonic and benthic foraminifera with variable diagenetic alteration stages have $\delta^{18}O$ values ranging from −1.70 ‰ to +0.40 ‰ and +2.10 ‰ to +3.76 ‰, respectively. With the increase of diagenetic alteration, the average values of $\delta^{18}O_{planktonic}$ reveal a slight positive bias, while the average values of $\delta^{18}O_{benthic}$ exhibit no significant variation.

4.3 Elemental compositions

EPMA maps of *G. menardii* and *N. dutertrei* serve to investigate the spatial variability of Mg/Ca in strongly altered tests (Figure 4). SEM images of a single sample reveal isolated calcite crystal overgrowth on the test wall cross-section (Figures 4A–C). The EPMA maps demonstrate clear Mg enrichment in the authigenic overgrowths. The highest Mg concentrations of the carbonate crystals encrusting on the outside and/or inside of the foraminiferal tests can reach up to 4.8 wt%, which is 4-10 times higher than the Mg content of the biogenic low-Mg calcite of the original test (Figures 4B–D).

In addition, LA-ICP-MS analyses were utilized to determine the elemental compositions of foraminiferal tests Appendix 3. Boxplots reveal the overall distributions of elemental ratios of foraminiferal tests at each diagenetic alteration stage (Figure 5). In general, Mg/Ca, V/Ca, Mn/Ca, Fe/Ca, Co/Ca, Cu/Ca, Ba/Ca, and U/Ca ratios increase strongly with the degree of diagenesis, Al/Ca, Ni/Ca, and Mo/Ca ratios increase moderately, and there is no significant change in Ni/Ca, Sr/Ca, and Cd/Ca ratios. Particularly noteworthy is the order-of-magnitude increase in Mg concentrations (Figure 5), yielding Mg/Ca values ranging from 0.85 for unaltered tests to 69.8 mmol/mol for strongly altered tests. For comparison, an earlier study reported Mg/Ca of 0.5 to 5 mmol/mol and 0.5 to 10 mmol/mol in pristine planktonic and benthic foraminifera, respectively (Lea, 2003).

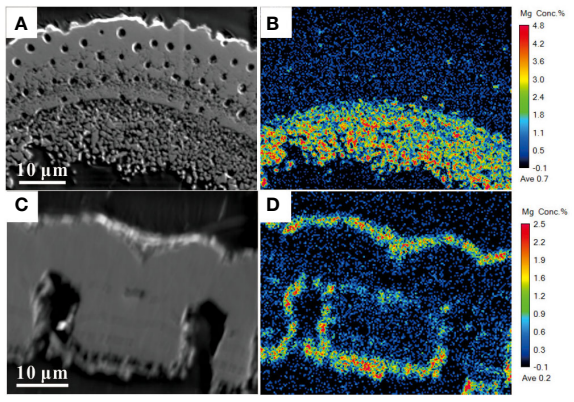

FIGURE 4
SEM images of foraminiferal wall cross-section and Mg (intensity) EPMA map of *G menardii* **(A, B)** and *N. dutertrei* **(C, D)**.

5 Discussion

5.1 Influence of diagenesis on foraminiferal tests

Based on petrographic evidence, diagenetic alteration of foraminiferal tests at Site GMGS2-16 is mostly due to calcite overgrowths (Figure 2). The secondary calcite crystals encrust test surfaces and fill test pores, leading to changes in the visual characteristics of the tests. With increased amounts of secondary calcite deposited on internal and/or external test surfaces and within pores, the color of foraminiferal tests changes to yellow or gray, the reflectance and transparency of the tests are reduced, and test walls start to display a 'frosty' texture.

Precipitation of inorganic calcite can alter the original geochemical composition of a foraminiferal test (Edgar et al., 2015). In a methane release environment, authigenic carbonate acquires substantial carbon from methane, which has a strongly ^{13}C-depleted signature (−110 ‰ to −50 ‰ for biogenic methane, and −50 ‰ to −30 ‰ for thermogenic methane), resulting in extremely low $\delta^{13}C$ values for MDAC (Whiticar, 1999; Chen et al., 2016b; Liang et al., 2017). MDAC precipitation can overprint the isotope signal of the pristine biogenic test, leading to bulk-test $\delta^{13}C$ values of −10 ‰ or lower (Torres et al., 2010). The authigenic carbonates of the study site precipitated in irregular clumps having extremely negative $\delta^{13}C$ (−37.3 ‰ to −51.7 ‰) and positive $\delta^{18}O$ values (+3.13 ‰ to +4.95 ‰), which is typical of MDAC (Zhao et al., 2018). We infer that methane release also caused secondary calcite precipitation on foraminiferal tests, leading to strongly negative $\delta^{13}C$ values (as low as −8.99‰) and weakly positive $\delta^{18}O$ values. Compared with the planktonic foraminiferal taxa, the $\delta^{18}O$ of the benthic taxon *U. peregrina* was less affected by MDAC precipitation, probably because the original oxygen isotopic composition of *U. peregrina* tests was similar to that of the secondary calcite.

Elemental compositions also provide evidence of diagenetic alteration due to methane release. Mg-rich carbonates having low $\delta^{13}C$ values are known to dominate in cold-seep settings (Schneider et al., 2017). In the vicinity of methane seeps, the Mg/Ca ratio of carbonate overgrowths on foraminiferal test walls can be as high as 220 mmol/mol, while the Mg/Ca ratio of the original test calcite is <10 mmol/mol (Panieri et al., 2017). As the degree of diagenetic alteration increases, Mg/Ca ratios rise and $\delta^{13}C$ declines, providing evidence of concurrent incorporation of Mg and ^{13}C-depleted carbon into secondary precipitates. This pattern is observed in the present study, in which Mg/Ca ratios are significantly negatively correlated with $\delta^{13}C$ ($R^2 = 0.32$, $p < 0.001$, $n = 51$) (Figure 6A).

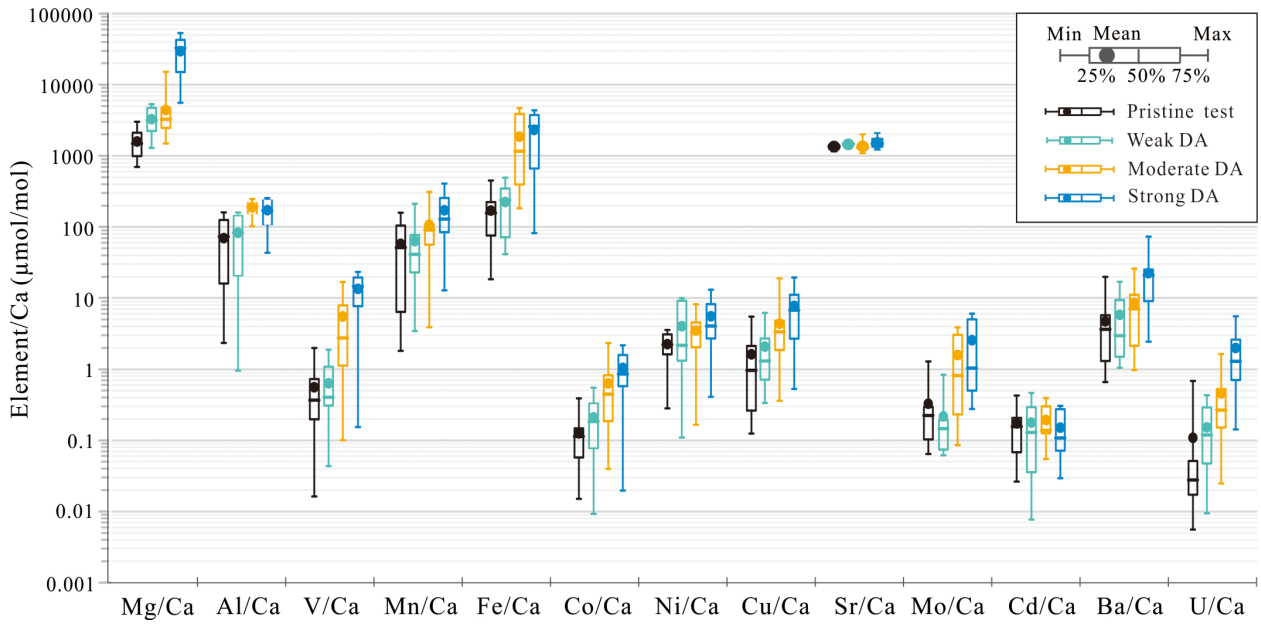

FIGURE 5
Boxplots of Element/Ca of foraminiferal specimens measured by LA-ICP-MS and tabulated according to degree of diagenetic alteration: pristine (black), weakly altered (green), moderately altered (orange), and strongly altered (blue).

Authigenic carbonate minerals precipitated in cold-seep systems include high-Mg calcite, aragonite, and dolomite (Greinert et al., 2013). The mineralogy of carbonate assemblages can be recognized by Sr/Ca versus Mg/Ca covariation patterns, as shown for Niger Delta sediments influenced by methane seepage (Figure 6B; Bayon et al., 2007). In the present study, pristine foraminiferal samples yield Sr/Ca and Mg/Ca ratios typical of biogenic calcite, whereas altered tests yield signals reflecting a mixture of biogenic calcite and high-Mg calcite (Figure 6B). With increasing diagenetic alteration, the average composition of the tests more closely approaches that of high-Mg calcite, indicating that it is the dominant secondary phase. Panieri et al. (2017) found that foraminiferal calcite and authigenic Mg-calcite crystals have identical lattice fringes, and, therefore, that foraminifera can serve as a nucleation template for authigenic Mg-calcite overgrowths.

The stratigraphic distribution of diagenetically altered foraminiferal tests at Site GMGS2-16 does not follow a regular pattern of increasing intensity with depth. Rather, there is a close association between intensely altered tests and authigenic carbonate nodules, which are present at 4.68, 10.83, 92.32, 140.18, 148.63, 149.67, 164.68, 192.46, and 205.8 mbsf (Figure 7). The percentage of altered foraminifera is obviously correlated with the content of carbonate nodules in these core samples (Zhao et al., 2018) ($y = 1.18x + 17.39$, $R^2 = 0.35$, $p = 0.04$, $n = 11$). The most likely explanation for this relationship is that formation of MDAC nodules and high-Mg calcite overgrowths on foraminifera was triggered by the same cause, i.e., a methane release event. However, diagenetically altered foraminifera are also present in intervals without authigenic carbonate nodules, such as at 50.47-69.68, 120.81-144.18, and 180.96-189.66 mbsf (Figure 7). We infer that this pattern is due to the high sensitivity of foraminiferal tests to methane, leading to secondary overgrowths at lower methane concentrations and/or during shorter periods of peak methane flow compared to MDAC precipitation.

Compared to the Sr/Ca of pristine foraminiferal tests (1.1-1.5 mmol/mol), the altered tests yield slightly higher values (1.1-2.1 mmol/mol), suggesting a limited increase in response to diagenetic alteration (Figure 6B). For primary carbonate phases, aragonite is typically enriched in Sr by a factor of 3-10× relative to calcite (Katz et al., 1972). In the methane release environment, aragonite is more inclined to precipitate near the sediment-water interface while calcite tends to form at greater depth, because the sulfate inhibition effect on calcite is stronger than on aragonite (Luff and Wallmann, 2003; Goetschl et al., 2019; Jin et al., 2021). Although cold seeps with high methane fluxes and, thus, shallow SMTZs are commonly characterized by aragonite precipitation (Burton, 1993; Bayon et al., 2007; Peckmann et al., 2009; Nöthen and Kasten, 2011), increases in both the Mg and Sr content of the study samples suggest precipitation of a secondary Mg-calcite phase that is enriched in Sr. During early diagenesis, aragonite can be replaced by more stable carbonate species, leading to Sr/Ca ratios above typical values for pristine calcite tests (Detlef et al., 2020). Sr enrichment may also be related to distortion of the calcite crystal lattice due to incorporation of Mg^{2+}, generating more space for relatively large Sr^{2+} cations (Mucci and Morse, 1983).

Cu was co-enriched with Mg, as shown by its positive correlation with Mg/Ca ($R^2 = 0.38$, $p < 0.001$, $n = 60$; Figure 8A). It is well known that Cu plays a central role in the metabolism of aerobic methane-oxidizing bacteria. When Cu is abundant, methanotrophic bacteria produce a membrane-bound Cu-containing enzyme (particulate methane mono-oxygenase) that catalyzes the oxidation of methane to methanol (Glass and

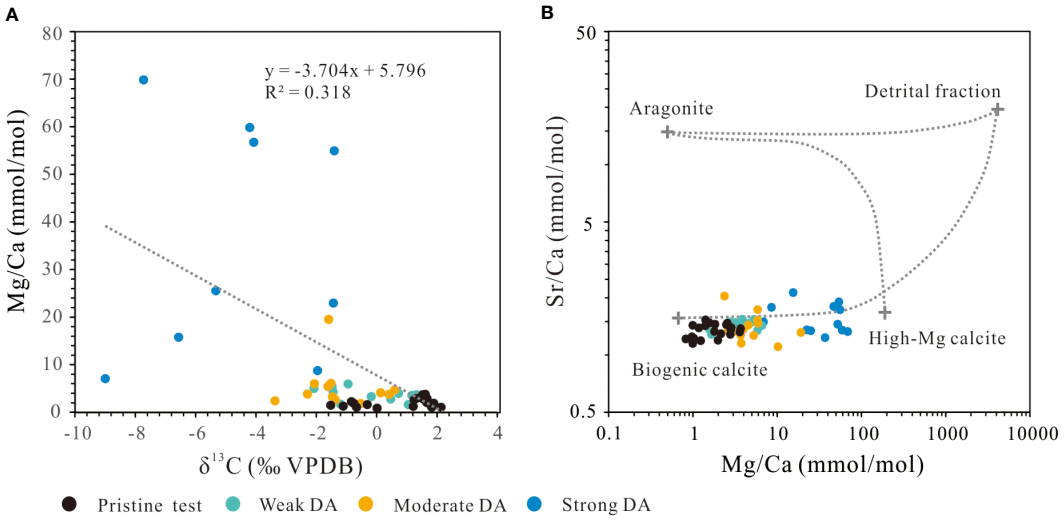

FIGURE 6
(A) Mg/Ca vs. $\delta^{13}C$ for various diagenetic alteration stages. **(B)** Sr/Ca vs. Mg/Ca for various diagenetic alteration stages. Endmember compositions of aragonite, high Mg-calcite, biogenic calcite, and the detrital fraction (black crosses), along with mixing trends (dashed curves) from Bayon et al. (2007).

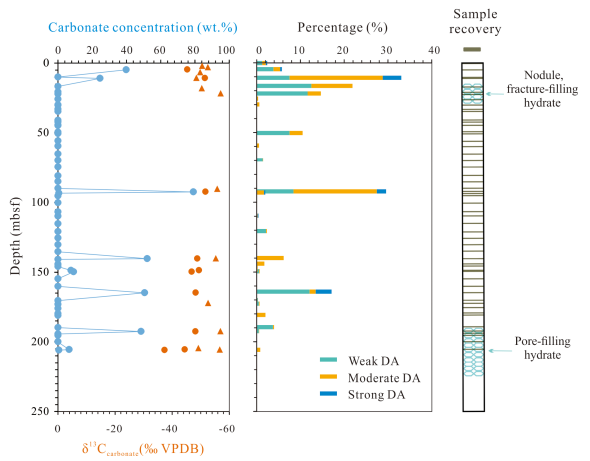

FIGURE 7
The distribution of foraminiferal tests by degree of diagenetic alteration (DA; this study), compared with the distribution and carbon isotope of carbonate nodules (Zhao et al., 2018) at Site GMGS2-16.

Orphan, 2012). Near the sediment-water interface, methane oxidation can be catalyzed by Cu-dependent aerobic methane-oxidizing bacteria, which may account for the high Cu contents of a few Sr-rich foraminiferal tests (e.g., the diagenetically altered test of *U. peregrina* from sample GMGS2-16B-1H-1a).

Foraminiferal Ba/Ca is positively correlated with Mg/Ca ratios (R^2 = 0.55, p < 0.001, n = 63) (Figure 8B). In the methane release environment, porewater Ba concentrations increase below the depth of sulfate depletion, and the consequent upward flux of dissolved Ba is almost quantitatively precipitated as authigenic barite at the SMTZ (Torres et al., 2002; Snyder et al., 2007). Carbonate samples from the Oregon Margin and foraminiferal samples from fossil methane seeps exposed from Oregon to Vancouver Island also show a trend of increasing Mg and Ba, consistent with barium incorporation into Mg-carbonates formed in methane-charged sediments (Torres et al., 2009; Torres et al., 2010).

Mn/Ca and Fe/Ca ratios also exhibit distinct increases from pristine to strongly altered tests. In the latter, Fe is the second most abundant cation with the Fe/Ca ratios of up to 4.6 mmol/mol, while Mn/Ca ratios are up to 0.49 mmol/mol. LA-ICP-MS results show a significant difference in the median values of Mn/Ca and Fe/Ca ratios in the moderate and strongly altered foraminifera compared with the pristine tests and positive correlations of Mn/Ca and Fe/Ca with Mg/Ca (R^2 = 0.31, p < 0.001, n = 63; R^2 = 0.25, p < 0.001, n = 63, respectively) (Figures 8D, E). However, the presence of Fe-Mn-oxides and pyrite in foraminiferal tests can bias LA-ICP-MS analyses of Mn/Ca and Fe/Ca. Since the cleaning process applied in this study may not completely eliminate detrital materials, Al/Ca and Mn/Ca were monitored to identify possible contamination from clays, silicate minerals, and Mn-Fe-oxide coatings (Lea, 2003). Specimens with values above 1 mmol/mol Mn/Ca or 0.25 mmol/mol Al/Ca (n.b., thresholds from Skinner et al., 2019) were removed from the dataset before statistical calculations to avoid potential effects linked to clay contamination. In the screened dataset, Al/Ca shows little correlation with Mg/Ca (R^2 = 0.08, p < 0.001, n = 63) (Figure 8C), supporting our inference of limited effects from detrital materials. On the other hand, if all foraminiferal Mn was derived from Mn-Fe-oxides, a Mn/Mg ratio close to that of global-ocean Mn-Fe-oxide crusts/nodules of 5 mol/mol would be expected (de

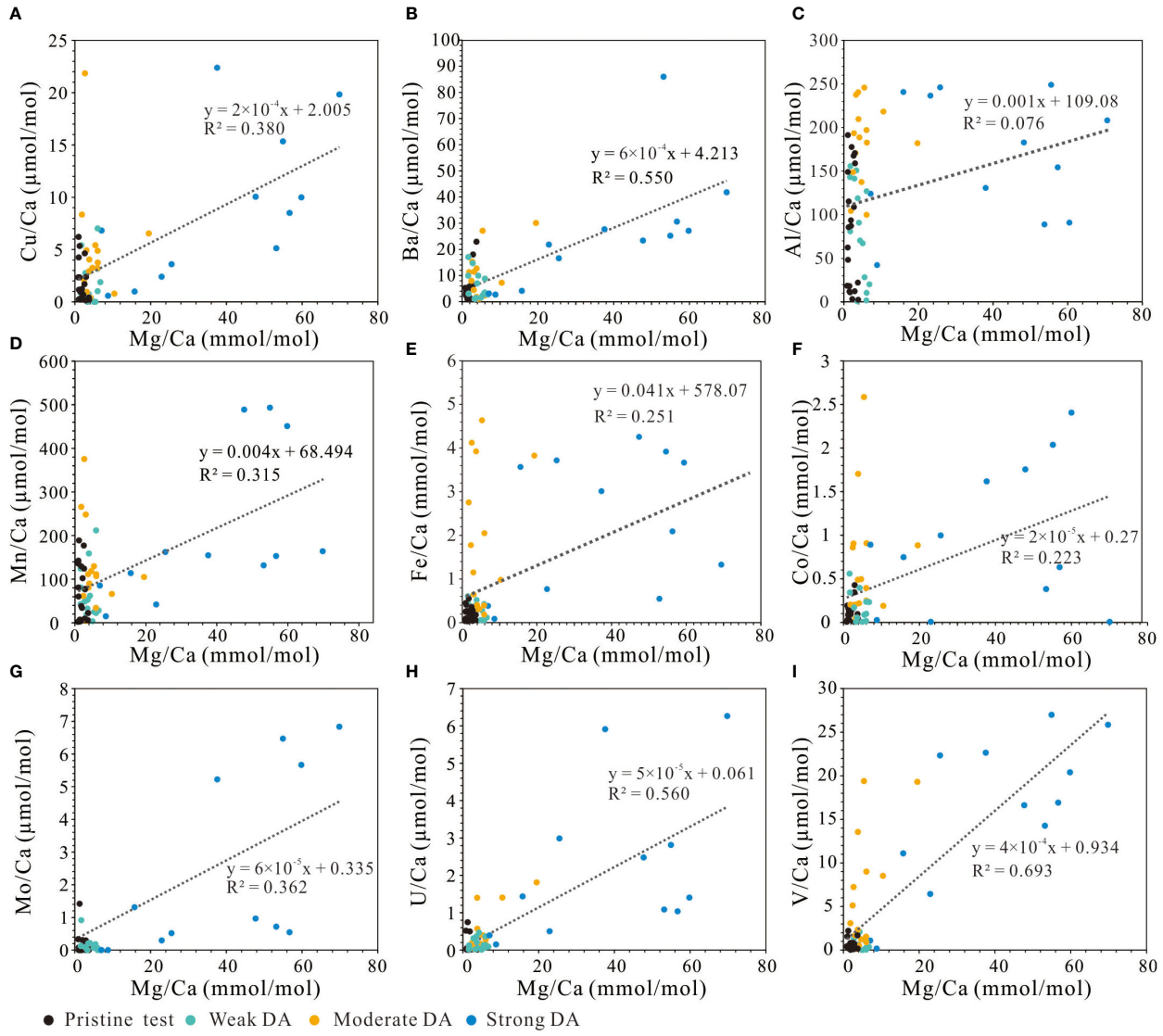

FIGURE 8
(A–I) Correlations of LA-ICP-MS foraminiferal elemental ratios. The samples are coded according to diagenetic alteration stage: pristine (black), weakly altered (green), moderately altered (orange), and strongly altered (blue).

Lange et al., 1992; Pattan, 1993). However, all of the study specimens have much lower Mn/Mg ratios (0.7-155 mmol/mol), suggesting that Mn-Fe-oxides are not an important contaminant phase.

SEM images of foraminifera from both above and below the SMTZ at Site GMGS2-16 demonstrate the presence of pyrite framboids within the foraminiferal tests, suggesting co-precipitation of authigenic carbonates and pyrite. The AOM reaction can lead to the production of pyrite (Lin et al., 2016). Authigenic pyrite framboids form in the spaces between calcite microcrystals of the overgrowths (Figures 2G1–2) and are not easily removed during cleaning processes, resulting in Fe contamination. Moreover, in the AOM process, anaerobic methanotrophic archaea (ANME) require large amounts of iron (Glass and Orphan, 2012), which can lead to further Fe enrichment of diagenetically altered foraminiferal tests.

The concentrations of trace elements such as Mo, U, V, Ni, Cd and Co are very sensitive to environmental conditions in siliciclastic depositional systems (Tribovillard et al., 2006; Guo et al., 2013; Wang et al., 2018). At Site GMGS2-16, significant differences in the medians of Mo/Ca, U/Ca, V/Ca, and Co/Ca are observed between moderately and strongly altered foraminifera (Figure 5). In addition, these Element/Ca ratios are significantly positively correlated with Mg/Ca (R^2 = 0.36, n = 50; R^2 = 0.56, n = 63; R^2 = 0.69, n = 62; R^2 = 0.22, n = 57, respectively; all $p < 0.001$) (Figures 8F–I). On the other hand, Ni/Ca and Cd/Ca show little relationship to the degree of diagenetic alteration, although this might be related to the lack of data for more than half of the samples in which the trace-element content is below the detection limit. The enrichment of these redox-sensitive elements in methane-derived carbonates compared to other types of marine carbonates has previously been ascribed to the ubiquitous presence of anoxic

conditions in the methane release environment (Tribovillard et al., 2006; Palomares et al., 2012; Sato et al., 2012; Hu et al., 2015; Chen et al., 2016b). Moreover, in addition to iron, other transition metals (Co, V, Mo) have been identified in proteins and enzymes involved in the metabolism of sulfate-reducing bacteria or methanogenic and methanotrophic archaea (Scheller et al., 2010; Glass and Orphan, 2012; Glass et al., 2014; Glass et al., 2018), which may account for the enrichment of these elements in the sediment.

5.2 Diagenetic processes and implications for paleo-methane release events

In this study, our results show that stable carbon and oxygen isotopes as well as elemental ratios (Mg/Ca, Sr/Ca, Ba/Ca, Mn/Ca, Fe/Ca, Mo/Ca, U/Ca, V/Ca, Ni/Ca, Co/Ca and Cu/Ca) measured in the foraminiferal tests are consistent with those of MDAC reported in earlier studies (see Section 5.1). Changes in geochemical compositions can provide valuable information, as they record fluid sources and biogeochemical processes during and after methane release.

Dissolved inorganic carbon (DIC) produced during AOM is typically characterized by highly ^{13}C-depleted carbon derived from methane (Haese et al., 2003; Yoshinaga et al., 2014), yielding extremely low δ^{13}C values. Variation in the elemental compositions of MDAC formed in various depositional environments is closely related to the dynamics of methane release (Feng et al., 2009).

Diagenetically altered foraminiferal tests from sample GMGS2-16B-1H-1a (0.23 mbsf), record extremely negative δ^{13}C values and enrichments in Mg/Ca, Sr/Ca, Ba/Ca, Mn/Ca, Fe/Ca, Mo/Ca, U/Ca, V/Ca, Ni/Ca, Co/Ca and Cu/Ca (Figure 9). This sample is located near the sediment-water interface, above the present SMTZ. In this sample, gypsum occurs on the exterior wall of foraminiferal test (Figure 2G3), indicating downward migration of the SMTZ, a process that caused anaerobic pyrite oxidation and gypsum formation at the previous (higher) level of the SMTZ. As mentioned above, aragonite precipitation is favored when the SMTZ is located at shallower depths, in response to a methane release event having high flow rates (Peckmann et al., 2001; Moore et al., 2004; Gieskes et al., 2005; Nöthen and Kasten, 2011; Hu et al., 2015; Jin et al., 2021). Overgrowth of Sr-enriched Mg-calcite possibly reflects recrystallization of primary aragonitic phases. Near the sediment-water interface, methane oxidation can be catalyzed by Cu-dependent aerobic methane-oxidizing bacteria, resulting in a concomitant increase in the contents of both Sr and Cu (Glass and Orphan, 2012). The foraminifera from sample GMGS2-16D-8H-1 (92.32 mbsf) have similar geochemical compositions (Figure 9) and contain gypsum (Figure 2G4), which may be evidence of another methane release event from near the sediment-water interface. Samples GMGS2-16D-2H-1 (10.83 mbsf), GMGS2-16F-6H-1 (50.47 mbsf) and GMGS2-16H-4H-1b (164.68 mbsf) show similar extremely negative δ^{13}C values and enrichments in Mg/Ca, Ba/Ca, Mn/Ca, Fe/Ca, Mo/Ca, U/Ca, V/Ca, Ni/Ca and Co/Ca, suggesting that a high-Mg calcite contaminant formed in the deeper SMTZ in association with low rates of methane-bearing fluid flow (Luff and Wallmann, 2003; Feng et al., 2009).

We infer that Mg enrichment of diagenetically altered foraminifera coupled with increases in Sr/Ca, Ba/Ca, Mn/Ca, Fe/Ca, Mo/Ca, U/Ca, V/Ca, Ni/Ca, Co/Ca and Cu/Ca ratios are potentially reliable indicators of paleo-methane release events. Furthermore, the main differences in elemental compositions of authigenic carbonate formed near the seafloor versus in deeper anoxic porewaters are higher concentrations of Cu and Sr in the former. For this reason, enrichments of Cu/Ca and Sr/Ca in diagenetically altered foraminiferal tests may be used to recognize intense upward methane fluxes within the sediment column.

Determining the timing of methane release events using stratigraphic data is difficult because the SMTZ can migrate vertically through the sediment column, leading to precipitation of MDAC overgrowths on foraminiferal tests at times younger than their stratigraphic ages. When a high methane flux produces a shallow SMTZ, the formation of secondary overgrowths can be considered quasi-synsedimentary, but otherwise the stratigraphic age of MDAC represents a maximum formation age. At the study site, stratigraphic ages were calculated by linear interpolation from the age framework established by Chen et al., 2016a. The two documented methane release events at 0.23 mbsf and 92.32 mbsf thus have maximum ages of ~0.47 ka and ~170 ka, respectively.

Based on the observations and analyses of foraminifera from Site GMGS2-16, a potential mechanism for diagenetic alteration of buried foraminiferal tests linked to the gas hydrate geosystem is proposed (Figure 10). When gas hydrates are in a stable state, there is no unusual methane emission, and the geochemical compositions of foraminifera record the original (i.e., unaltered) signal of normal marine conditions (Figure 10A; sample GMGS2-16F-2P-CC and GMGS2-16F-5H-2). During a high methane flux event, methane is transported further towards the sediment-water interface, shifting the SMTZ upward and compressing it into the uppermost sediment column (Figure 10B; sample GMGS2-16B-1H-1a and GMGS2-16D-8H-1). The authigenic carbonates (mainly Sr-enriched Mg-calcite) with extremely negative δ^{13}C values and enrichments in Mg/Ca, Sr/Ca, Ba/Ca, Mn/Ca, Fe/Ca, Mo/Ca, U/Ca, V/Ca, Ni/Ca, Co/Ca and Cu/Ca, are co-precipitated with pyrite in the SMTZ near the seafloor. When the methane flux is subsequently reduced, the SMTZ migrates back downward to a greater depth in the sediment column (e.g., similar to the depth of the current SMTZ at the study site). In this scenario, authigenic pyrites and carbonates (mainly high-Mg calcite) formed in anoxic porewaters are characterized by extremely negative δ^{13}C values and enrichments in Mg/Ca, Ba/Ca, Mn/Ca, Fe/Ca, Mo/Ca, U/Ca, V/Ca, Ni/Ca and Co/Ca. In the upper part of the sediment column, carbonate and pyrite precipitated before the downward shift of the SMTZ are converted to authigenic gypsum through anaerobic pyrite oxidation (Figure 10C; samples GMGS2-16D-2H-1, GMGS2-16F-6H-1, and GMGS2-16H-4H-1b).

6 Conclusions

In this study, we used a suite of petrographic and geochemical analyses (including reflected light microscopy, SEM imaging,

10.3389/fmars.2023.1166305

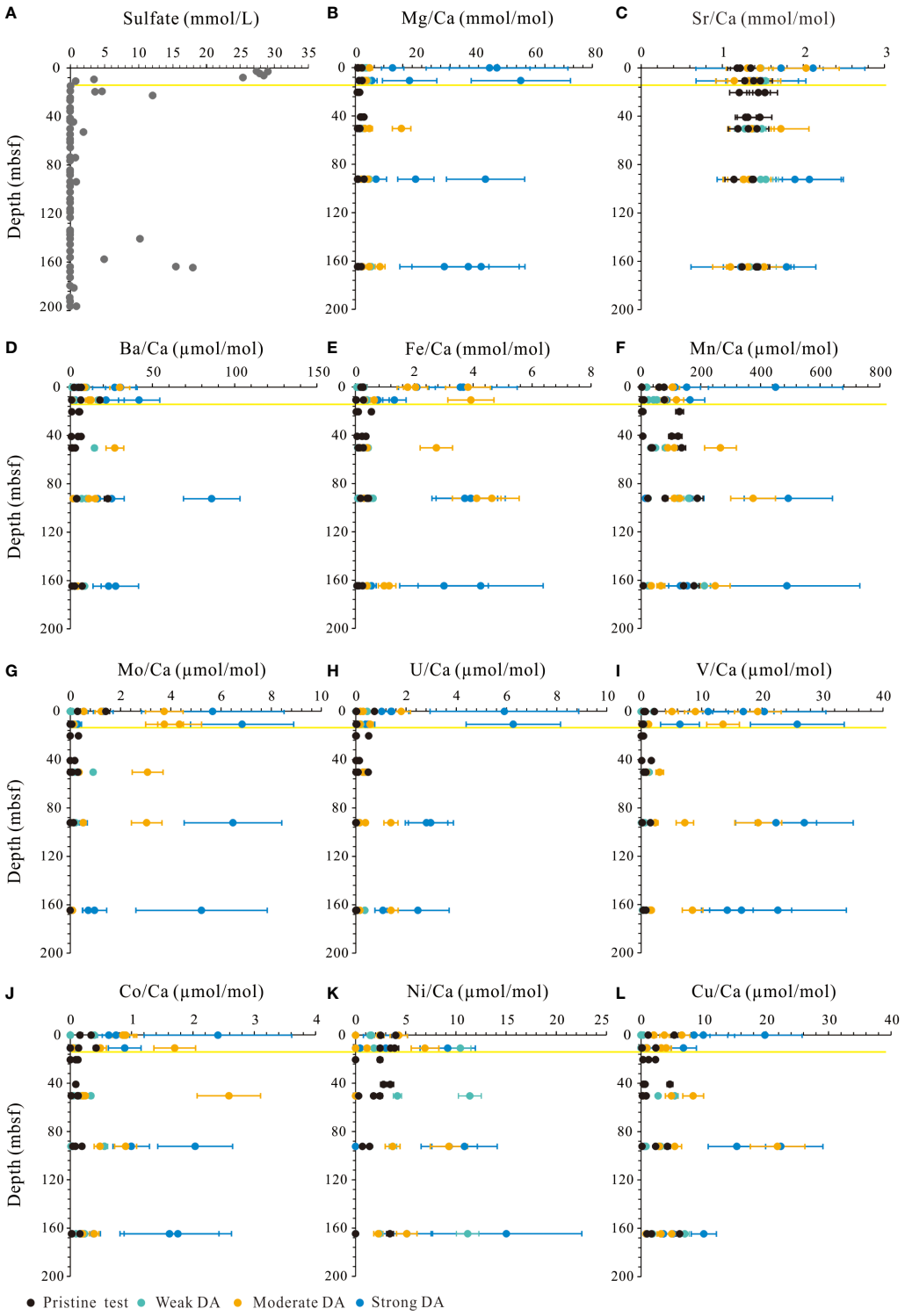

FIGURE 9
Sulfate **(A)** (Kuang et al., 2018) and elemental-ratio **(B–L)** profiles for Site GMGS2-16. The samples are coded according to diagenetic alteration stage: pristine (black), weakly altered (green), moderately altered (orange), and strongly altered (blue). Error bars represent one standard deviation. The yellow lines show the depth of the current sulfate-methane interface (SMI; i.e., where porewater sulfate declines to zero).

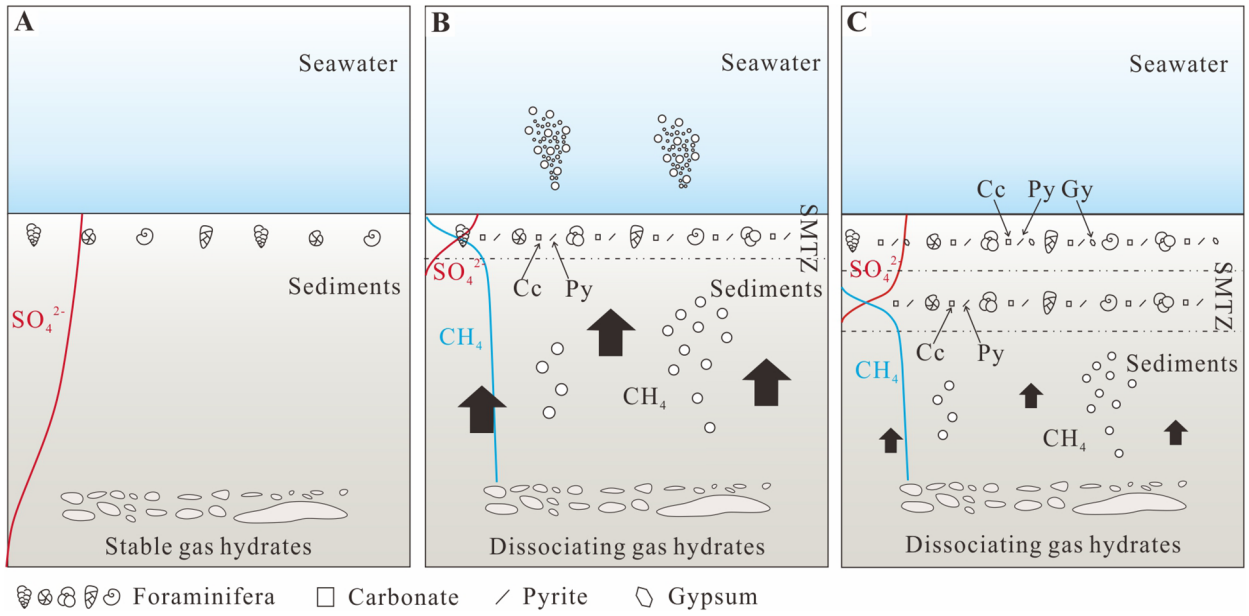

FIGURE 10
Schematic of post-depositional alteration of buried foraminiferal tests in a gas hydrate geosystem (modified from Kennett et al., 2000). **(A)** Gas hydrates are in a stable state, and the geochemical compositions of foraminifera record the original signal of the normal marine conditions. **(B)** During a high methane flux event, methane is transported further toward the sediment-water interface, shifting the SMTZ upward and compressing it into the uppermost sediment column. Authigenic carbonates are co-precipitated with pyrite in the SMTZ near the seafloor, causing foraminiferal shells buried in this interval to be coated with MDAC, along with some framboidal pyrite interspersed between carbonate crystals. **(C)** Subsequent reduction of the methane flux causes the SMTZ to migrate back downward within the sediment column. Authigenic pyrite and carbonate form in the active SMTZ, whereas pyrite precipitated in the upper part of the sediment column before the downward SMTZ shift are converted to authigenic gypsum through anaerobic pyrite oxidation, which also leaves traces on foraminiferal shells. Cc, carbonate; Py, pyrite; Gy, gypsum.

oxygen and carbon isotopic measurements, LA-ICP-MS, and EPMA elemental mapping) to study foraminiferal tests from gas hydrate-bearing sediments of the northern South China Sea that exhibit varying degrees of diagenetic alteration. Our goals were to make inferences on the post-burial alteration processes affecting foraminiferal calcite caused by methane release. Our results are consistent with diagenetically altered foraminiferal tests acting as a template for MDAC precipitation. The $\delta^{13}C$ values and Mg/Ca ratios of tests are susceptible to diagenetic alteration. There is a negative correlation between $\delta^{13}C$ values and the degree of diagenetic alteration, but a positive correlation with Mg/Ca ratios. This may be related to the relative contribution of Mg-calcite, which has a strongly negative $\delta^{13}C$ value, to bulk foraminiferal carbonate. The elemental content of diagenetically altered foraminifera can be used to reconstruct methane release history. We infer that enrichments in Mg along with increased Ba/Ca, Mn/Ca, Fe/Ca, Mo/Ca, U/Ca, V/Ca, Ni/Ca and Co/Ca ratios are potentially reliable indicators of paleo-methane release events. Furthermore, enrichments of Cu/Ca and Sr/Ca may be used to recognize episodes of intense methane flux. Reconstruction of the methane release history of Site GMGS2-16 reveals that diagenetically altered foraminifera record frequent fluctuations of the SMTZ, indicating a variable methane flux intensity. Notably, the methane release events have maximum ages of ~0.47 ka and ~170 ka.

Data availability statement

The original contributions presented in the study are included in the article/Supplementary Material. Further inquiries can be directed to the corresponding author.

Author contributions

YC and JW designed the study. YC and JW collected the samples. YC, ZW, XM, and CC have carried out the laboratory work and analyzed the data. YC, JW, and TA wrote the manuscript. All authors contributed to the article and approved the submitted version.

Funding

This research was supported by the National Natural Science Foundation of China (No. 42276068), China National Gas Hydrate Project (Grant No. DD20160211) and State Key Laboratory of Marine Geology, Tongji University (No. MGK202206).

Acknowledgments

We would like to acknowledge the crew and scientists of the GMGS2 expedition for their supports in sediment samples and analyses. We are grateful to Profs. Huiming Bao and Yongbo Peng for technical support in stable isotope analysis and Hongfang Chen for support in the LA-ICP-MS and EPMA analysis. We acknowledge the editors and reviewers for their constructive reviews.

Conflict of interest

The authors declare that the research was conducted in the absence of any commercial or financial relationships that could be construed as a potential conflict of interest.

Publisher's note

Supplementary material

The Supplementary Material for this article can be found online at: https://www.frontiersin.org/articles/10.3389/fmars.2023.1166305/full#supplementary-material

References

Bayon, G., Lemaitre, N., Barrat, J.-A., Wang, X., Feng, D., and Duperron, S. (2020). Microbial utilization of rare earth elements at cold seeps related to aerobic methane oxidation. *Chem. Geology* 555, 119832. doi: 10.1016/j.chemgeo.2020.119832

Bayon, G., Pierre, C., Etoubleau, J., Voisset, M., Cauquil, E., Marsset, T., et al. (2007). Sr/Ca and Mg/Ca ratios in Niger delta sediments: Implications for authigenic carbonate genesis in cold seep environments. *Mar. Geology* 241, 93–109. doi: 10.1016/j.margeo.2007.03.007

Borrelli, C., Gabitov, R. I., Liu, M.-C., Hertwig, A. T., and Panieri, G. (2020). The benthic foraminiferal $\delta^{34}S$ records flux and timing of paleo methane emissions. *Sci. Rep.* 10, 1304. doi: 10.1038/s41598-020-58353-4

Burton, E. A. (1993). Controls on marine carbonate cement mineralogy: review and reassessment. *Chem. Geology* 105, 163–179. doi: 10.1016/0009-2541(93)90124-2

Cen, Y., Wang, J., Ding, X., Stow, D., Wang, Z., Chen, C., et al. (2022). Tracing the methane events by stable carbon isotopes of benthic foraminifera at glacial periods in the Andaman Sea. *J. Earth Sci.* 33 (6), 1571–1582. doi: 10.1007/s12583-022-1750-x

Chen, F., Hu, Y., Feng, D., Zhang, X., Cheng, S., Cao, J., et al. (2016b). Evidence of intense methane seepages from molybdenum enrichments in gas hydrate-bearing sediments of the northern south China Sea. *Chem. Geology* 443, 173–181. doi: 10.1016/j.chemgeo.2016.09.029

Chen, L., Liu, Y. S., Hu, Z. C., Gao, S., Zong, K. Q., and Chen, H. (2011). Accurate determinations of fifty-four major and trace elements in carbonate by LA-ICP-MS using normalization strategy of bulk components as 100%. *Chem. Geology* 284, 283–295. doi: 10.1016/j.chemgeo.2011.03.007

Chen, F., Zhuang, C., Zhou, Y., Su, X., Duan, J., Liu, G. H., et al. (2016a). Calcareous nannofossils and foraminifera biostratigraphy on the northeastern slope of the south China Sea and variation in sedimentation rates. *Earth Sci.* 41 (3), 416–424. doi: 10.3799/dqkx.2016.033

Crémière, A., Lepland, A., Chand, S., Sahy, D., Condon, D. J., Noble, S. R., et al. (2016). Timescales of methane seepage on the Norwegian margin following collapse of the Scandinavian ice sheet. *Nat. Commun.* 7, 11509. doi: 10.1038/ncomms11509

de Lange, G. J., van Os, B., and Poorter, R. (1992). Geochemical composition and inferred accretion rates of sediments and managanese nodules from a submarine hill in the Madeira abyssal plain, eastern north Atlantic. *Mar. Geology* 109, 171–194. doi: 10.1016/0025-3227(92)90227-9

Detlef, H., Sosdian, S. M., Kender, S., Lear, C. H., and Hall, I. R. (2020). Multi-elemental composition of authigenic carbonates in benthic foraminifera from the eastern Bering Sea continental margin (International ocean discovery program site U1343). *Geochimica Cosmochimica Acta* 268, 1–21. doi: 10.1016/j.gca.2019.09.025

Dickens, G. R., Castillo, M. M., and Walker, J. C. G. (1997). A blast of gas in the latest Paleocene: Simulating first-order effects of massive dissociation of oceanic methane hydrate. *Geology* 25, 259–262. doi: 10.1130/0091-7613(1997)025<0259:ABOGIT>2.3.CO;2

Edgar, K. M., Anagnostou, E., Pearson, P. N., and Foster, G. L. (2015). Assessing the impact of diagenesis on $\delta^{11}B$, $\delta^{13}C$, $\delta^{18}O$, Sr/Ca and B/Ca values in fossil planktic foraminiferal calcite. *Geochimica Cosmochimica Acta* 166, 189–209. doi: 10.1016/j.gca.2015.06.018

Feng, D., Chen, D., and Roberts, H. H. (2009). Petrographic and geochemical characterization of seep carbonate from bush hill (GC 185) gas vent and hydrate site of the gulf of Mexico. *Mar. Petroleum Geology* 26, 1190–1198. doi: 10.1016/j.marpetgeo.2008.07.001

Feng, J.-C., Wang, Y., Li, X.-S., Li, G., Zhang, Y., and Chen, Z.-Y. (2015). Production performance of gas hydrate accumulation at the GMGS2-site 16 of the pearl river mouth basin in the south China Sea. *J. Natural Gas Sci. Eng.* 27, 306–320. doi: 10.1016/j.jngse.2015.08.071

Fontanier, C., Dissard, D., Ruffine, L., Mamo, B., Ponzevera, E., Pelleter, E., et al. (2018). Living (stained) deep-sea foraminifera from the Sea of marmara: A preliminary study. *Deep Sea Res. Part II: Topical Stud. Oceanography* 153, 61–78. doi: 10.1016/j.dsr2.2017.12.011

Friedrich, O., Schiebel, R., Wilson, P. A., Weldeab, S., Beer, C. J., Cooper, M. J., et al. (2012). Influence of test size, water depth, and ecology on Mg/Ca, Sr/Ca, $\delta^{18}O$ and $\delta^{13}C$ in nine modern species of planktic foraminifers. *Earth Planetary Sci. Lett.* 319–320, 133–145. doi: 10.1016/j.epsl.2011.12.002

Gieskes, J., Mahn, C., Day, S., Martin, J. B., Greinert, J., Rathburn, T., et al. (2005). A study of the chemistry of pore fluids and authigenic carbonates in methane seep environments: Kodiak trench, hydrate ridge, Monterey bay, and eel river basin. *Chem. Geology* 220, 329–345. doi: 10.1016/j.chemgeo.2005.04.002

Glass, J. B., Chen, S., Dawson, K. S., Horton, D. R., Vogt, S., Ingall, E. D., et al. (2018). Trace metal imaging of sulfate-reducing bacteria and methanogenic archaea at single-cell resolution by synchrotron X-ray fluorescence imaging. *Geomicrobiology J.* 35, 81–89. doi: 10.1101/087585

Glass, J. B., and Orphan, V. J. (2012). Trace metal requirements for microbial enzymes involved in the production and consumption of methane and nitrous oxide. *Front. Microbiol.* 3. doi: 10.3389/fmicb.2012.00061

Glass, J. B., Yu, H., Steele, J. A., Dawson, K. S., Sun, S., Chourey, K., et al. (2014). Geochemical, metagenomic and metaproteomic insights into trace metal utilization by methane-oxidizing microbial consortia in sulphidic marine sediments. *Environ. Microbiol.* 16, 1592–1611. doi: 10.1111/1462-2920.12314

Goetschl, K. E., Purgstaller, B., Dietzel, M., and Mavromatis, V. (2019). Effect of sulfate on magnesium incorporation in low-magnesium calcite. *Geochimica Cosmochimica Acta* 265, 505–519. doi: 10.1016/j.gca.2019.07.024

Gong, J., Sun, X., Xu, L., and Lu, H. (2017). Contribution of thermogenic organic matter to the formation of biogenic gas hydrate: Evidence from geochemical and microbial characteristics of hydrate-containing sediments in the taixinan basin, south China Sea. *Mar. Petroleum Geology* 80, 432–449. doi: 10.1016/j.marpetgeo.2016.12.019

Greinert, J., Bohrmann, G., and Suess, E. (2013). "Gas hydrate-associated carbonates and methane-venting at hydrate ridge: Classification, distribution, and origin of authigenic lithologies," in *Natural gas hydrates: Occurrence, distribution, and detection*, vol. 124 . Eds. C. K. Paull and W. P. Dillon (Washington, DC: American Geophysical Union), 99–113.

Guo, H., Du, Y., Lian, Z., Yang, J., Huang, H., Liu, M., et al. (2013). Trace and rare earth elemental geochemistry of carbonate succession in the middle gaoyuzhuang formation, pingquan section: Implications for early mesoproterozoic ocean redox conditions. *J. Palaeogeogr.* 2 (2), 209–221. doi: 10.3724/SP.J.1261.2013.00027

Haese, R. R., Meile, C., Van Cappellen, P., and De Lange, G. J. (2003). Carbon geochemistry of cold seeps: Methane fluxes and transformation in sediments from kazan mud volcano, eastern Mediterranean Sea. *Earth Planetary Sci. Lett.* 212, 361–375. doi: 10.1016/S0012-821X(03)00226-7

Hill, T. M., Kennett, J. P., and Valentine, D. L. (2004). Isotopic evidence for the incorporation of methane-derived carbon into foraminifera from modern methane seeps, hydrate ridge, northeast pacific. *Geochimica Cosmochimica Acta* 68, 4619–4627. doi: 10.1016/j.gca.2004.07.012

Hu, Y., Feng, D., Liang, Q., Xia, Z., Chen, L., and Chen, D. (2015). Impact of anaerobic oxidation of methane on the geochemical cycle of redox-sensitive elements at

cold-seep sites of the northern south China Sea. *Deep Sea Res. Part II: Topical Stud. Oceanography* 122, 84–94. doi: 10.1016/j.dsr2.2015.06.012

Jørgensen, B. B. (2021). Sulfur biogeochemical cycle of marine sediments. *Geochemical Perspect.* 10 (2), 145–307. doi: 10.7185/geochempersp.10.2

Jin, M., Feng, D., Huang, K., Peckmann, J., Li, N., Huang, H., et al. (2021). Behavior of mg isotopes during precipitation of methane-derived carbonate: Evidence from tubular seep carbonates from the south China Sea. *Chem. Geology* 567, 120101. doi: 10.1016/j.chemgeo.2021.120101

Katz, A., Sass, E., Starinsky, A., and Holland, H. D. (1972). Strontium behavior in the aragonite-calcite transformation: An experimental study at 40–98 c. *Geochimica Cosmochimica Acta* 36 (4), 481–496. doi: 10.1016/0016-7037(72)90037-3

Kennett, J. P., Cannariato, K. G., Hendy, I. L., and Behl, R. J. (2000). Carbon isotopic evidence for methane hydrate instability during quaternary interstadials. *Science* 288, 128–133. doi: 10.1126/science.288.5463.128

Kuang, Z., Fang, Y., Liang, J., and Wang, L. (2018). Geomorphological-geological-geophysical signatures of high-flux fluid flows in the eastern pearl river mouth basin and effects on gas hydrate accumulation. *Sci. China Earth Sci.* 61, 914–924. doi: 10.1007/s11430-017-9183-y

Lea, D. W. (2003). "Trace elements in foraminiferal calcite," in *Modern foraminifera*. Ed. B. K. S. Gupta (Dordrecht: Kluwer Academic Publishers), 259–277.

Liang, Q., Hu, Y., Feng, D., Peckmann, J., Chen, L., Yang, S., et al. (2017). Authigenic carbonates from newly discovered active cold seeps on the northwestern slope of the south China Sea: Constraints on fluid sources, formation environments, and seepage dynamics. *Deep Sea Res. Part I: Oceanographic Res. Papers* 124, 31–41. doi: 10.1016/j.dsr.2017.04.015

Lin, Z., Sun, X., Strauss, H., Lu, Y., Böttcher, M. E., Teichert, B. M. A., et al. (2018). Multiple sulfur isotopic evidence for the origin of elemental sulfur in an iron-dominated gas hydrate-bearing sedimentary environment. *Mar. Geology* 403, 271–284. doi: 10.1016/j.margeo.2018.06.010

Lin, Q., Wang, J., Algeo, T. J., Su, P., and Hu, G. (2016). Formation mechanism of authigenic gypsum in marine methane hydrate settings: Evidence from the northern south China Sea. *Deep Sea Res. Part I: Oceanographic Res. Papers* 115, 210–220. doi: 10.1016/j.dsr.2016.06.010

Liu, Y., Hu, Z., Gao, S., Günther, D., Xu, J., Gao, C., et al. (2008). *In situ* analysis of major and trace elements of anhydrous minerals by LA-ICP-MS without applying an internal standard. *Chem. Geology* 257, 34–43. doi: 10.1016/j.chemgeo.2008.08.004

Liu, Y., Wei, J., Li, Y., Chang, J., Miao, X., and Lu, H. (2022). Seep dynamics as revealed by authigenic carbonates from the eastern qiongdongnan basin, south China Sea. *Mar. Petroleum Geology* 142, 105736. doi: 10.1016/j.marpetgeo.2022.105736

Luff, R., and Wallmann, K. (2003). Fluid flow, methane fluxes, carbonate precipitation and biogeochemical turnover in gas hydrate-bearing sediments at hydrate ridge, cascadia margin: numerical modeling and mass balances. *Geochimica Cosmochimica Acta* 67, 3403–3421. doi: 10.1016/s0016-7037(03)00127-3

Martin, R. A., Nesbitt, E. A., and Campbell, K. A. (2007). Carbon stable isotopic composition of benthic foraminifera from pliocene cold methane seeps, cascadia accretionary margin. *Palaeogeography Palaeoclimatology Palaeoecol.* 246, 260–277. doi: 10.1016/j.palaeo.2006.10.002

Miao, X., Feng, X., Li, J., and Lin, L. (2021). Tracing the paleo-methane seepage activity over the past 20,000 years in the sediments of qiongdongnan basin, northwestern south China Sea. *Chem. Geology* 559, 119956. doi: 10.1016/j.chemgeo.2020.119956

Millo, C., Sarnthein, M., Erlenkeuser, H., and Frederichs, T. (2005a). Methane-driven late pleistocene $\delta^{13}C$ minima and overflow reversals in the southwestern Greenland Sea. *Geology* 33, 873. doi: 10.1130/G21790.1

Millo, C., Sarnthein, M., Erlenkeuser, H., Grootes, P. M., and Andersen, N. (2005b). Methane-induced early diagenesis of foraminiferal tests in the southwestern Greenland Sea. *Mar. Micropaleontology* 58, 1–12. doi: 10.1016/j.marmicro.2005.07.003

Moore, T. S., Murray, R. W., Kurtz, A. C., and Schrag, D. P. (2004). Anaerobic methane oxidation and the formation of dolomite. *Earth Planetary Sci. Lett.* 229, 141–154. doi: 10.1016/j.epsl.2004.10.015

Morley, C. K. (2012). Late Cretaceous–early palaeogene tectonic development of SE Asia. *Earth-Science Rev.* 115, 37–75. doi: 10.1016/j.earscirev.2012.08.002

Mucci, A., and Morse, J. W. (1983). The incorporation of Mg^{2+} and Sr^{2+} into calcite overgrowths: influences of growth rate and solution composition. *Mar. Geology* 47, 217–233. doi: 10.1016/0016-7037(83)90135-7

Nöthen, K., and Kasten, S. (2011). Reconstructing changes in seep activity by means of pore water and solid phase Sr/Ca and Mg/Ca ratios in pockmark sediments of the northern Congo fan. *Mar. Geology* 287, 1–13. doi: 10.1016/j.margeo.2011.06.008

Palomares, R. M., Hernández, R. L., and Frías, J. M. (2012). Mechanisms of trace metal enrichment in submarine, methane-derived carbonate chimneys from the gulf of cadiz. *J. Geochemical Explor.* 112, 297–305. doi: 10.1111/1462-2920.12314

Panieri, G., James, R. H., Camerlenghi, A., Westbrook, G. K., Consolaro, C., Cacho, I., et al. (2014). Record of methane emissions from the West Svalbard continental margin during the last 23.500yrs revealed by $\delta^{13}C$ of benthic foraminifera. *Global Planetary Change* 122, 151–160. doi: 10.1016/j.gloplacha.2014.08.014

Panieri, G., Lepland, A., Whitehouse, M. J., Wirth, R., Raanes, M. P., James, R. H., et al. (2017). Diagenetic mg-calcite overgrowths on foraminiferal tests in the vicinity of methane seeps. *Earth Planetary Sci. Lett.* 458, 203–212. doi: 10.1016/j.gloplacha.2014.08.014

Pattan, J. N. (1993). Manganese micronodules: a possible indicator of sedimentary environments. *Mar. Geology* 113, 331–344. doi: 10.1016/0025-3227(93)90026-R

Peckmann, J., Birgel, D., and Kiel, S. (2009). Molecular fossils reveal fluid composition and flow intensity at a Cretaceous seep. *Geology* 37, 847–850. doi: 10.1130/G25658A.1

Peckmann, J., Reimer, A., Luth, U., Luth, C., Hansen, B. T., Heinicke, C., et al. (2001). Methane-derived carbonates and authigenic pyrite from the northwestern black Sea. *Mar. Geology* 177, 129–150. doi: 10.1016/S0025-3227(01)00128-1

Peckmann, J., and Thiel, V. (2004). Carbon cycling at ancient methane–seeps. *Chem. Geology* 205, 443–467. doi: 10.1016/j.chemgeo.2003.12.025

Rathmann, S., Hess, S., Kuhnert, H., and Mulitza, S. (2004). Mg/Ca ratios of the benthic foraminifera *Oridorsalis umbonatus* obtained by laser ablation from core top sediments: Relationship to bottom water temperature. *Geochemistry Geophysics Geosystems* 5, Q12013. doi: 10.1029/2004GC000808

Retallack, G. J., Seyodolali, A., Krull, E. S., Holser, W., Ambers, C. P., and Kyte, F. T. (1998). Search for evidence of impact at the permian-Triassic boundary in Antarctica and Australia. *Geology* 26, 979–982. doi: 10.1130/0091-7613(1998)0262.3.CO;2

Sato, H., Hayashi, K. I., Ogawa, Y., and Kawamura, K. (2012). Geochemistry of deep sea sediments at cold seep sites in the nankai trough: insights into the effect of anaerobic oxidation of methane. *Mar. Geology* 323–325, 47–55. doi: 10.1016/j.margeo.2012.07.013

Scheller, S., Goenrich, M., Boecher, R., Thauer, R. K., and Jaun, B. (2010). The key nickel enzyme of methanogenesis catalyses the anaerobic oxidation of methane. *Nature* 465, 606–608. doi: 10.1038/nature09015

Schier, K., Himmler, T., Lepland, A., Kraemer, D., Schönenberger, J., and Bau, M. (2021). Insights into the REY inventory of seep carbonates from the northern Norwegian margin using geochemical screening. *Chem. Geology* 559, 119857. doi: 10.1016/j.chemgeo.2020.119857

Schlanger, S. O., and Douglas, R. G. (1974). "The pelagic ooze-chalk-limestone transition and its implication for marine stratigraphy," in *Pelagic sediments: on land and under the Sea*. Eds. K. J. Hsü and H. C. Jenkyns (London: Blackwell Scientific Publications), 117–148.

Schneider, A. (2018). Diagenetically altered benthic foraminifera reveal paleo-methane seepage, department of geoscience (Norway: The Arctic University of Norway).

Schneider, A., Crémière, A., Panieri, G., Lepland, A., and Knies, J. (2017). Diagenetic alteration of benthic foraminifera from a methane seep site on vestnesa ridge (NW Svalbard). *Deep Sea Res. Part I: Oceanographic Res. Papers* 123, 22–34. doi: 10.1016/j.dsr.2017.03.001

Skinner, L. C., Sadekov, A., Brandon, M., Greaves, M., Plancherel, Y., de la Fuente, M., et al. (2019). Rare earth elements in early-diagenetic foraminifer 'coatings': Pore-water controls and potential palaeoceanographic applications. *Geochimica Cosmochimica Acta* 245, 118–132. doi: 10.1016/j.gca.2018.10.027

Snyder, G. T., Dickens, G. R., and Castellini, D. G. (2007). Labile barite contents and dissolved barium concentrations on Blake ridge: New perspectives on barium cycling above gas hydrate systems. *J. Geochemical Explor.* 95, 48–65. doi: 10.1016/j.gexplo.2007.06.001

Sztybor, K., and Rasmussen, T. L. (2017). Diagenetic disturbances of marine sedimentary records from methane-influenced environments in the fram strait as indications of variation in seep intensity during the last 35 000 years. *Boreas* 46, 212–228. doi: 10.1111/bor.12202

Taylor, B., and Hayes, D. E. (1980). "The tectonic evolution of the south China basin," in *The tectonic and geologic evolution of southeast Asian seas and islands*, vol. 23. Ed. D. E. Hayes (Washington, DC: American Geophysical Union), 89–104.

Them, T. R., Gill, B. C., Caruthers, A. H., Gerhardt, A. M., Gröcke, D. R., Lyons, T. W., et al. (2018). Thallium isotopes reveal protracted anoxia during the toarcian (early Jurassic) associated with volcanism, carbon burial, and mass extinction. *Proc. Natl. Acad. Sci. (U.S.A.)* 115 (26), 6596–6601. doi: 10.1073/pnas.1803478115

Torres, M. E., Embley, R. W., Merle, S. G., Trehu, A. M., Collier, R. W., Suess, E., et al. (2009). Methane sources feeding cold seeps on the shelf and upper continental slope off central Oregon, USA. *Geochemistry Geophysics Geosystems* 10, Q11003. doi: 10.1029/2009GC002518

Torres, M. E., Martin, R. A., Klinkhammer, G. P., and Nesbitt, E. A. (2010). Post depositional alteration of foraminiferal shells in cold seep settings: New insights from flow-through time-resolved analyses of biogenic and inorganic seep carbonates. *Earth Planetary Sci. Lett.* 299, 10–22. doi: 10.1016/j.epsl.2010.07.048

Torres, M. E., McManus, J., and Huh, C. A. (2002). Fluid seepage along the San clemente fault scarp: basin-wide impact on barium cycling. *Earth Planetary Sci. Lett.* 203, 181–194. doi: 10.1016/S0012-821X(02)00800-2

Tribovillard, N., Algeo, T. J., Lyons, T., and Riboulleau, A. (2006). Trace metals as paleoredox and paleoproductivity proxies: an update. *Chem. Geology* 232, 12–32. doi: 10.1016/j.chemgeo.2006.02.012

Wan, S., Feng, D., Chen, F., Zhuang, C., and Chen, D. (2018). Foraminifera from gas hydrate-bearing sediments of the northeastern south China Sea: Proxy evaluation and application for methane release activity. *J. Asian Earth Sci.* 168, 125–136. doi: 10.1016/j.jseaes.2018.04.036

Wang, Z., Wang, J., Fu, X., Zhan, W., Armstrong-Altrin, J. S., Yu, F., et al. (2018). Geochemistry of the upper Triassic black mudstones in the qiangtang basin, Tibet: Implications for paleoenvironment, provenance, and tectonic setting. *J. Asian Earth Sci.* 76, 346–361. doi: 10.1016/j.jseaes.2018.04.022

Whiticar, M. J. (1999). Carbon and hydrogen isotope systematics of bacterial formation and oxidation of methane. *Chem. Geology* 161, 291–314. doi: 10.1016/S0009-2541(99)00092-3

Yoshinaga, M. Y., Holler, T., Goldhammer, T., Wegener, G., Pohlman, J. W., Brunner, B., et al. (2014). Carbon isotope equilibration during sulphate-limited anaerobic oxidation of methane. *Nat. Geosci.* 7, 190–194. doi: 10.1038/NGEO2069

Zhang, G., Liang, J., Lu, J. A., Yang, S., Zhang, M., Holland, M., et al. (2015). Geological features, controlling factors and potential prospects of the gas hydrate occurrence in the east part of the pearl river mouth basin, south China Sea. *Mar. Petroleum Geology* 67, 356–367. doi: 10.1016/j.marpetgeo.2015.05.021

Zhao, J., Wang, J., Cen, Y., Su, P., Lin, Q., and Liu, J. (2018). Authigenic minerals at site GMGS2-16 of northeastern south China Sea and its implications for gas hydrate evolution. *Mar. Geology Quaternary Geology* 38 (5), 144–155. doi: 10.16562/j.cnki.0256-1492.2018.05.014

Zhao, J., Wang, J., Phillips, S. C., Liang, J., Su, P., Lin, Q., et al. (2021). Non-evaporitic gypsum formed in marine sediments due to sulfate-methane transition zone fluctuations and mass transport deposits in the northern south China Sea. *Mar. Chem.* 233, 103988. doi: 10.1016/j.marchem.2021.103988

Zhu, B., Ge, L., Yang, T., Jiang, S., and Lv, X. (2019). Stable isotopes and rare earth element compositions of ancient cold seep carbonates from enza river, northern Apennines (Italy): Implications for fluids sources and carbonate chimney growth. *Mar. Petroleum Geology* 109, 434–448. doi: 10.1016/j.marpetgeo.2019.06.033

Zhu, W., Huang, B., Mi, L., Wilkins, R. W. T., Fu, N., and Xiao, X. (2009). Geochemistry, origin, and deep-water exploration potential of natural gases in the pearl river mouth and qiongdongnan basins, south China Sea. *AAPG Bull.* 93, 741–761. doi: 10.1306/02170908099